

New $z > 7$ Lyman-alpha Emitters in EGS: Evidence of an Extended Ionized Structure at $z \sim 7.7$

INTAE JUNG,^{1,2,3} STEVEN L. FINKELSTEIN,⁴ REBECCA L. LARSON,^{4,*} TAYLOR A. HUTCHISON,^{2,†} AMBER N. STRAUGHN,²
MICAELA B. BAGLEY,⁴ MARCO CASTELLANO,⁵ NIKKO J. CLERI,^{6,7} M. C. COOPER,⁸ MARK DICKINSON,⁹ HENRY C. FERGUSON,¹
BENNE W. HOLWERDA,¹⁰ JEYHAN S. KARTALTEPE,¹¹ SEONWOO KIM,¹² ANTON M. KOEKEMOER,¹ CASEY PAPOVICH,^{6,7}
HYUNBAE PARK,^{13,14} LAURA PENTERICCI,⁵ PABLO G. PÉREZ-GONZÁLEZ,¹⁵ MIMI SONG,¹⁶ SANDRO TACCHELLA,^{17,18}
BENJAMIN J. WEINER,¹⁹ CHRISTOPHER N. A. WILLMER,²⁰ AND JORGE A. ZAVALA²¹

¹Space Telescope Science Institute, 3700 San Martin Drive Baltimore, MD 21218, USA

²Astrophysics Science Division, NASA Goddard Space Flight Center, 8800 Greenbelt Rd, Greenbelt, MD 20771, USA

³Department of Physics, The Catholic University of America, Washington, DC 20064, USA

⁴Department of Astronomy, The University of Texas at Austin, Austin, TX, USA

⁵INAF - Osservatorio Astronomico di Roma, via di Frascati 33, 00078 Monte Porzio Catone, Italy

⁶Department of Physics and Astronomy, Texas A&M University, College Station, TX, 77843-4242 USA

⁷George P. and Cynthia Woods Mitchell Institute for Fundamental Physics and Astronomy, Texas A&M University, College Station, TX, 77843-4242 USA

⁸Department of Physics & Astronomy, University of California, Irvine, 4129 Reines Hall, Irvine, CA 92697, USA

⁹NSF's National Optical-Infrared Astronomy Research Laboratory, 950 N. Cherry Ave., Tucson, AZ 85719, USA

¹⁰Physics & Astronomy Department, University of Louisville, 40292 KY, Louisville, USA

¹¹Laboratory for Multiwavelength Astrophysics, School of Physics and Astronomy, Rochester Institute of Technology, 84 Lomb Memorial Drive, Rochester, NY 14623, USA

¹²Department of Astronomy, University of Illinois, 1002 West Green Street, Urbana, IL 61801, USA

¹³Lawrence Berkeley National Laboratory, CA 94720, USA

¹⁴Berkeley Center for Cosmological Physics, UC Berkeley, CA 94720, USA

¹⁵Centro de Astrobiología (CAB), CSIC-INTA, Ctra. de Ajalvir km 4, Torrejón de Ardoz, E-28850, Madrid, Spain

¹⁶Department of Astronomy, University of Massachusetts, Amherst, MA, 01002, USA

¹⁷Kavli Institute for Cosmology, University of Cambridge, Madingley Road, Cambridge, CB3 0HA, UK

¹⁸Cavendish Laboratory, University of Cambridge, 19 JJ Thomson Avenue, Cambridge, CB3 0HE, UK

¹⁹MMT/Steward Observatory, University of Arizona, 933 N. Cherry Ave., Tucson, AZ 85721, USA

²⁰Steward Observatory, University of Arizona, 933 N. Cherry Ave., Tucson, AZ, 85721, USA

²¹National Astronomical Observatory of Japan, 2-21-1 Osawa, Mitaka, Tokyo 181-8588, Japan

Submitted to the Astrophysical Journal

ABSTRACT

We perform a ground-based near-infrared spectroscopic survey using the Keck/MOSFIRE spectrograph to target Ly α emission at $7.0 < z < 8.2$ from 61 galaxies to trace the ionization state of the intergalactic medium (IGM). We cover a total effective sky area of $\sim 10' \times 10'$ in the Extended Groth Strip field of the Cosmic Assembly Near-infrared Deep Extragalactic Legacy Survey. From our observations, we detect Ly α emission at a $>4\sigma$ level in eight $z > 7$ galaxies, which include additional members of the known $z \sim 7.7$ Ly α -emitter (LAE) cluster (Tilvi et al. 2020). With the addition of these newly-discovered $z \sim 7.7$ LAEs, this is currently the largest measured LAE cluster at $z > 7$. The unusually-high Ly α detection rate at $z \sim 7.7$ in this field suggests significantly stronger Ly α emission from the clustered LAEs than from the rest of our targets. We estimate the ionized bubble sizes around these LAEs and conclude that the LAEs are clustered within an extended ionized structure created by overlapping ionized bubbles which allow the easier escape of Ly α from galaxies. It is remarkable that the brightest object in the cluster has the lowest measured redshift of the Ly α line, being placed in front of the other LAEs in the line-of-sight direction. This suggests that we are witnessing the enhanced IGM transmission of Ly α from galaxies on the rear side of an ionized area. This could be a consequence of Ly α

radiative transfer: Ly α close to the central velocity is substantially scattered by the IGM while Ly α from the rear-side galaxies is significantly redshifted to where it has a clear path.

1. Introduction

Investigating the ionization state of the intergalactic medium (IGM) during the epoch of reionization is critical to understanding the formation and evolution of galaxies in the early Universe. Along with contributions from active galactic nucleus (AGN) activity (e.g., Matsuoka et al. 2018; Kulkarni et al. 2019; Dayal et al. 2020), galaxies are responsible for supplying the bulk of ionizing photons into the IGM at early cosmic time (e.g., Robertson et al. 2015; McQuinn 2016; Dayal & Ferrara 2018; Finkelstein et al. 2019; Robertson 2021).

Lyman-alpha (Ly α) emission has been used as an observational probe of the ionization state of the IGM during the epoch of reionization (e.g., Miralda-Escudé & Rees 1998; Rhoads & Malhotra 2001; Stark et al. 2011; Pentericci et al. 2011; Dijkstra et al. 2014). A rapid decline in the Ly α fraction¹ at $z > 6$ suggests that the Ly α visibility is strongly affected by the IGM attenuation into the epoch of reionization (extensively reviewed by Ouchi et al. 2020, and the references therein) while the evolutionary effect of host galaxy properties could impact the observed evolution of Ly α (e.g., Mesinger et al. 2015; Hassan & Gronke 2021).

Thanks to the infrared (IR) wavelength coverage of JWST, it has become possible to deliver spectroscopic confirmations of reionization-era galaxies by detecting additional emission lines, which – in contrast to Ly α – are not affected by the neutral IGM (e.g., Brinchmann 2022; Schaerer et al. 2022; Trump et al. 2022; Trussler et al. 2022). As expected, Ly α emission has not been detected from the recent JWST NIR-Spec observations of $z > 9$ galaxies (Roberts-Borsani et al. 2022a; Williams et al. 2022; Curtis-Lake et al. 2022; Wang et al. 2022). This suggests that the sizes of ionized bubbles around these galaxies might not yet be sufficiently large enough to allow for the escape of Ly α , and their rapid growth has not yet occurred in this early stage of reionization.

At later stages of reionization, Ly α may become increasingly visible as ionized bubbles around galaxies grow over time. While a dearth of Ly α emission detected at $z > 8$ implies a significantly-neutral IGM in the early stage of reionization (a handful of detections reported in Zitrin et al. 2015; Laporte et al. 2017; Larson et al. 2022), a significant number of Ly α -emission lines have been detected at $z \gtrsim 7$, preferentially in UV-luminous galaxies (Oesch et al. 2015; Roberts-Borsani et al. 2016; Zheng et al. 2017; Castellano et al. 2018;

Tilvi et al. 2020; Jung et al. 2020; Hu et al. 2021; Jung et al. 2022; Endsley et al. 2021a; Endsley & Stark 2022). Thus, Ly α observations in the middle/late phases of reionization play a key role in tracing the evolution of ionized structures in the IGM.

Specifically, spectroscopic searches for Ly α in the middle phase of reionization at $z \sim 7 - 8$ provide a higher detection rate of Ly α particularly from UV-brighter galaxies (e.g., Jung et al. 2022, and references mentioned above), compared to rarer detections from fainter ones (Hoag et al. 2019; Roberts-Borsani et al. 2022b). This may indicate an inhomogeneous process of reionization where ionizing photons from UV-luminous galaxies in overdense regions are likely to ionize the IGM around them earlier than isolated UV-fainter galaxies (e.g., Mesinger et al. 2011; Ocvirk et al. 2021; Kannan et al. 2022). A continuing effort for Ly α observations is necessary to capture the global evolution of reionization, probing volumes larger than local ionized structures.

In this paper, we present new spectroscopic observations of reionization-era galaxies. Our study provides spectral coverage for Ly α emission from a large number of high-redshift candidate galaxies in a section of the Cosmic Assembly Near-infrared Deep Extragalactic Legacy Survey (CANDELS Grogin et al. 2011; Koekemoer et al. 2011) Extended Groth Strip (EGS) field, with a total effective area of $\sim 10' \times 10'$. Our spectroscopic observations deliver new Ly α emission lines detected from $z > 7$ galaxies, uncovering the largest LAE cluster² system in this early Universe at $z > 7$. The observations suggest that there is an extended ionized structure associated with the clustered LAEs, which enhances the transmission of Ly α along our line of sight. Non-detections of Ly α from the bulk of our targets reinforce earlier indications that the IGM at $z > 7$ is on average more neutral than at lower redshifts.

This paper is structured as follows. In Section 2, we describe our spectroscopic targets, MOSFIRE observations, and data reduction. We present the Ly α -emission lines detected in our observations, giving the measured physical properties of these emission lines and their host galaxies in Section 3. Section 4 discusses the extended ionized structure around the clustered LAEs at $z \sim 7.7$ in the EGS field. We then summarize our findings in Section 5. In this work, we assume the Planck cosmology (Planck Collaboration et al. 2016) with $H_0 = 67.8 \text{ km s}^{-1} \text{ Mpc}^{-1}$, $\Omega_M = 0.308$, and $\Omega_\Lambda = 0.692$. We use pMpc to indicate proper distances and cMpc to

* NSF Graduate Fellow

† NASA Postdoctoral Fellow

¹ Ly α fraction is defined as $N_{\text{LAE}}/N_{\text{LBG}}$, where N_{LAE} is the number of Ly α -detected objects and N_{LBG} is the number of high-redshift-candidate Lyman-Break Galaxies (LBGs) observed in spectroscopic observations.

² To clarify, our discussion on LAE clusters must be distinguished from the conventional definition of galaxy clusters in the context of forming virialized systems. Instead, we discuss LAE clusters whose LAEs overlap individual ionized bubbles each other, forming contiguous ionized areas.

indicate co-moving distances. The Hubble Space Telescope (HST) F606W, F814W, F105W, F125W, F140W, and F160W bands are referred to as V_{606} , I_{814} , Y_{105} , J_{125} , JH_{140} and H_{160} , respectively. All magnitudes in this work are quoted in the AB system (Oke & Gunn 1983), and all errors mentioned in this paper represent 1σ uncertainties (or central 68% confidence ranges) unless stated otherwise.

2. Data

2.1. Targets

Targets were selected from the photometrically-selected high-redshift galaxy catalog of Finkelstein et al. (2022), which is based on the updated HST CANDELS photometry. The photometric selection of high-redshift galaxies is done as described in Section 3.2 in Finkelstein et al. (2015), using the photometric redshift (z_p) probability distribution functions (PDFs) of $P(z)$ calculated by EAZY (Brammer et al. 2008). Then, we created a target list of $J_{125} \lesssim 27$ galaxies with $z_p > 6$ in the CANDELS/EGS field, which was used for designing optimized slitmask configurations in MAGMA³ for our Keck/MOSFIRE observations. In our slitmask design, we prioritized targets on slits based on the galaxy brightness (J_{125}) and the integrals of $P(z)$ in $7.0 < z < 8.2$, which corresponds to the MOSFIRE Y-band wavelength coverage for Ly α emission. This resulted in 61 Ly α targets across our four MOSFIRE pointings.

2.2. Photometric Data and Galaxy Properties

We use the photometric catalog of Finkelstein et al. (2022), which includes the HST ACS and WFC3 broadband photometry (V_{606} , I_{814} , Y_{105} , J_{125} , JH_{140} , and H_{160}) in addition to Spitzer/IRAC 3.6 μ m and 4.5 μ m band fluxes in the CANDELS/EGS field. We also use photometric redshift measurements that have been obtained with EAZY in Finkelstein et al. (2022) based on the updated CANDELS photometry.

To derive galaxy physical properties, we performed spectral energy distribution (SED) fitting with the photometric data to galaxy SED models. In the construction of galaxy model SEDs, we assume a Salpeter (1955) initial mass function with a stellar mass range of $0.1\text{--}100M_{\odot}$. We allow a range of metallicity from $0.005Z_{\odot}$ to $1.0Z_{\odot}$, and exponential models of star formation histories are used with exponentially varying timescales, parameterized with $\tau = 10$ Myr, 100 Myr, 1 Gyr, 10 Gyr, 100 Gyr, -300 Myr, -1 Gyr, -10 Gyr. We use the Calzetti (2001) dust attenuation description for a ranging from 0 to 0.8 mag in $E(B - V)$ values. Nebular emission lines are added, based on the Inoue (2011) emission-line ratio, through the same process as done in Salmon et al. (2015). The IGM attenuation was applied to model the galaxy SEDs, following Madau (1995).

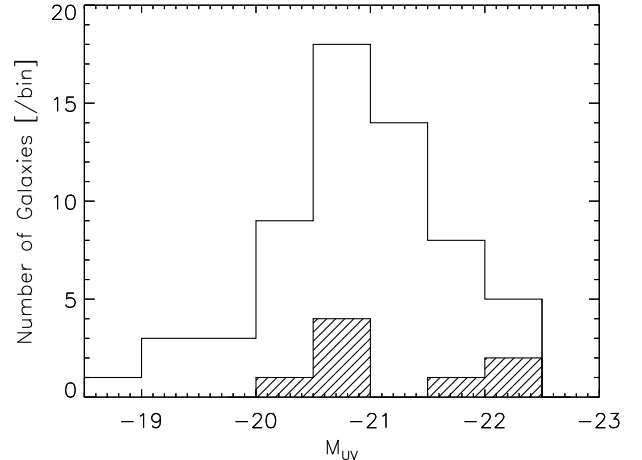


Figure 1. M_{UV} distribution of galaxies targeted in our MOSFIRE observations. A majority of the targets (>90%) are relatively UV bright with $M_{UV} \lesssim -20$, which is comparable to the detection limit of the CANDELS/HST J_{125} imaging depth in the EGS field. The shaded histogram indicates the M_{UV} of the sources with new Ly α detections.

Fiducial values of SED-derived physical properties, such as stellar masses, the absolute UV magnitudes (M_{UV}), and the UV continuum slope (β), were obtained from the best-fit models, which minimize χ^2 to the observed photometry. We estimated the uncertainties of physical quantities from SED fitting with 1000 Monte Carlo (MC) realizations of the simulated photometric fluxes, which we perturbed the observed fluxes with their photometric errors. The 1σ uncertainties denote the upper and lower limits of the central 68% range taken from the 1000 MC simulations. We repeated the process for all individual targets. We fixed galaxy redshifts with Ly α -derived spectroscopic redshifts for emission-detected objects and with the best-fit photometric redshifts for non-detection objects. We derived M_{UV} by averaging fluxes over a 100 \AA -bandpass (at the rest-frame 1450 – 1550 \AA) from SED models, which are not dust-corrected. The rest-frame UV continuum (β) was measured in the rest-frame UV bandpass of 1300 – 2600 \AA from the best-fit SED models as well, where β is the spectral index in the form of $f_{\lambda} \propto \lambda^{\beta}$.

We present the M_{UV} distribution of our targets in Figure 1. Our targets are somewhat biased toward UV-brighter galaxies, and a majority of the targets have $M_{UV} \lesssim -20$, comparable to the CANDELS/HST J_{125} imaging depth in the EGS field. Figure 2 presents our targets in the $M_{\text{star}}\text{--}M_{UV}$ plane (top) and their rest-UV continuum slope (β) versus M_{UV} (bottom). Although our sample contains limited coverage of UV-faint ($M_{UV} > -20$) sources, our spectroscopic targets are broadly consistent with the $z \sim 7$ $M_{\text{star}}\text{--}M_{UV}$ relation (Song et al. 2016b), which is representative of the typical high-redshift galaxy population. Also, we find the me-

³ <https://www2.keck.hawaii.edu/inst/mosfire/magma.html>

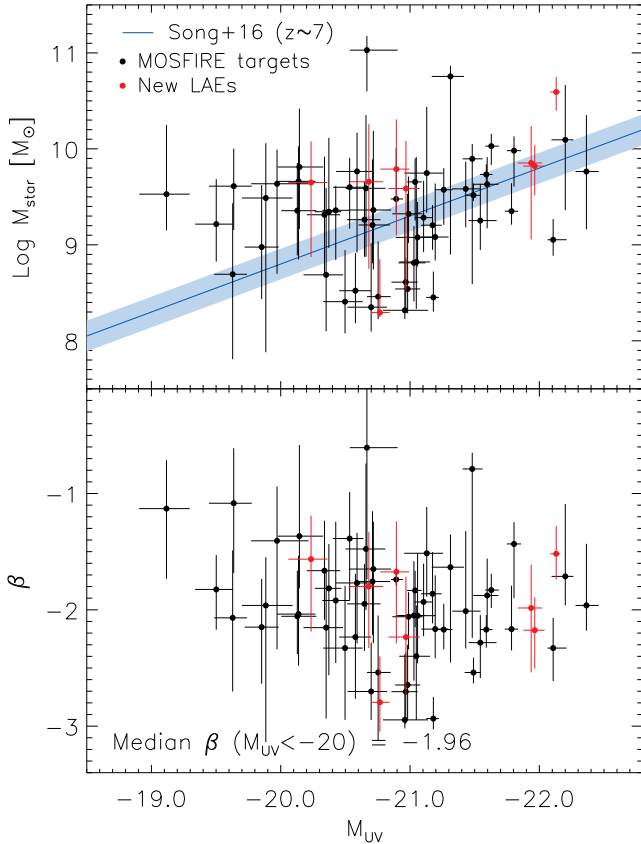


Figure 2. (Top) Our spectroscopic targets presented in the $M_{\text{star}}-M_{\text{UV}}$ plane. The blue line with shaded region shows the $z \sim 7$ $M_{\text{star}}-M_{\text{UV}}$ relation in Song et al. (2016b). (Bottom) The measurements of the rest-UV continuum slope (β) versus M_{UV} . The red symbols represent Ly α -detected targets.

dian value of the rest-UV continuum slopes at $\beta = -1.96$ from $M_{\text{UV}} < -20$ galaxies. This is comparable to the typical range of the UV slope measurements at this redshift (e.g., Finkelstein et al. 2012 find $\beta = -2.15^{+0.25}_{-0.16}$ for $M_{\text{UV}} < -20$ at $z = 7$).

2.3. MOSFIRE Y -band Observations in EGS

Spectroscopic observations of our sample were obtained over two nights in April 2021 using the Keck MOSFIRE spectrograph (McLean et al. 2012). This observing time was awarded through the NASA/Keck allocation (PI: I. Jung). We created four slitmask configurations that accommodate 61 high-redshift candidate galaxies for Ly α emission within a total effective sky area of $\sim 10' \times 10'$ (Figure 3). We observed two pointings each night, resulting in ~ 3.5 hr of total exposure time per mask. We used the Y -band filter to cover Ly α at $7.0 < z < 8.2$. The spectral resolution of the Y -band filter is $\sim 3\text{\AA}$ ($R = 3500$), and the slit width was set to be $0''.7$, which corresponds to the typical seeing level at Mauna Kea. During the observations, individual science frames were taken with 180-sec exposures, and we used a

standard ABAB dither pattern ($+1''.25, -1''.25, +1''.25, -1''.25$). The seeing level varies through the nights from $0''.7$ to $1''.2$. The observational details are listed in Table 1.

2.4. Data Reduction and Flux Calibration

We used the recent version of the public MOSFIRE data reduction pipeline (DRP)⁴ to reduce the raw data. The public DRP provides a sky-subtracted, flat-fielded, and rectified two-dimensional (2D) slit spectrum per slit object. The reduced spectra are wavelength-calibrated using telluric sky emission lines. Reduced 2D spectra have the spectral resolution of $1.09\text{\AA pixel}^{-1}$ and the spatial resolution of $0''.18 \text{ pixel}^{-1}$.

It has been reported that there is significant slit drift in the spatial direction (up to $\sim \text{pixel hr}^{-1}$) in previous MOSFIRE observations (e.g., Kriek et al. 2015; Song et al. 2016a; Jung et al. 2019; Hutchison et al. 2020; Larson et al. 2022), which needs to be handled separately if observations last longer than a couple of hours of exposure time. However, the general use of the public DRP is not aimed to correct the known slit drift in the spatial direction for long-exposure science. We corrected the slit drifts found in our observations, following Jung et al. (2020). Briefly, we reduced each adjacent pair of science frames with the public DRP separately, generating the reduced 2D spectra of 360 sec exposure time. In our observations, we placed slits on two faint stars per slitmask for flux calibration and used them to trace the slit drifts in individual MOSFIRE pointings as well. The amount of slit drift is estimated by tracing the spatial positions of slit continuum sources on the DRP-reduced 2D spectra of 360-sec exposure. We corrected the measured slit drifts when combining 360-sec DRP-reduced 2D spectra to generate a single science frame for each slit target. Cosmic ray rejection and/or bad pixel cleaning are not feasible with the DRP runs on a pair of science frames. Thus, we cleaned them by taking sigma-clipped means in the 2D combination step. Also, to maximize a resulting signal-to-noise ratio (SNR), we weight the DRP-reduced frames with the Gaussian peak fluxes of the slit stars, which reflect observing conditions.

The one-dimensional (1D) spectra of our slit objects were extracted from the combined 2D spectra using an optimal extraction scheme (Horne 1986) with a $1''.4$ spatial window twice the typical seeing level of Mauna Kea. We model a spatial weight profile that follows the spatial profile of the slit stars, thus the pixels near the peak of the stellar spatial profile are maximally weighted. This enables us to correct the offsets of the actual spatial locations of slit objects from the expected positions, which are found up to a couple of pixels in a spatial direction.

⁴ <https://keck-datareductionpipelines.github.io/MosfireDRP/>

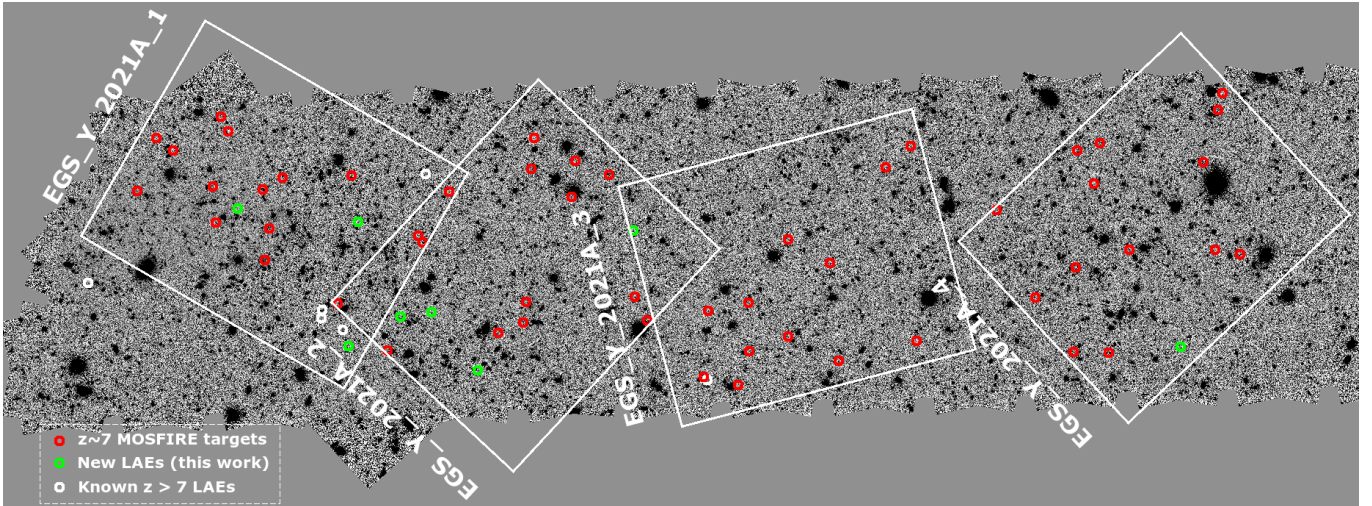


Figure 3. Four MOSFIRE mask configurations (white rectangles) overlaid in the CANDELS EGS H_{160} -band image. Our high-redshift spectroscopic targets for $\text{Ly}\alpha$ are shown as red circles, and the newly-detected $z > 7$ LAEs in this work are marked as green circles. We show the known $z > 7$ LAEs in EGS as white circles (Zitrin et al. 2015; Oesch et al. 2015; Roberts-Borsani et al. 2016; Tilvi et al. 2020; Larson et al. 2022).

Table 1. Summary of Keck/MOSFIRE Observations in EGS

Mask Name	R.A. (J2000.0)	Decl. (J2000.0)	Observational Date	N_{targets}	t_{exp}	Seeing ^a	Standard Star ^b
	(degree)	(degree)			(hr)	(arcsec)	
EGS_Y_2021A_1	215.11787	53.03937	2021 Apr 23	17	3.5	0.7	HIP56147
EGS_Y_2021A_2	215.05683	52.95982	2021 Apr 23	16	3.2	0.9	HIP56147
EGS_Y_2021A_3	214.95563	52.89208	2021 Apr 24	13	3.6	1.2	HIP56147
EGS_Y_2021A_4	214.80996	52.80919	2021 Apr 24	15	3.4	1.0	HIP56147

^aFull-width half maximum (FWHM) estimated from continuum objects in science mask configurations.

^bStandard star in our long-slit observations for flux calibration, listed in the *Hipparcos* index (van Leeuwen 2007).

The reduced 1D spectra were used to search for emission-line candidates. For the detection candidates, we repeated 1D extraction by shifting the centers of the optimal 1D extraction within ± 3 pixels from the corrected spatial locations of our slit objects. This accounts for the uncertainties in the centering of the objects' spatial locations, allowing us to obtain maximum SNRs of the emission-line candidates.

For absolute flux calibration and telluric absorption correction, we used long-slit observations of a spectro-photometric standard star (HIP56147, the spectral type A0V) and Kurucz (1993) model stellar spectra. We estimated a wavelength-dependent response curve each night by dividing the model stellar spectrum with the reduced long-slit stellar spectra. The response curves were scaled to match the known photometric magnitude of the standard star. However, our science observations were obtained in different observing conditions, such as seeing and airmass, to the standard star observations.

Thus, we estimated additional scaling factors using slit stars in the science slitmasks to refine the absolute flux calibration by matching their Y -band magnitudes measured from our spectra to the known Y_{105} magnitudes from the existing HST photometry (Finkelstein et al. 2022). The additional scaling factors were at the level of $< 10\%$. The slit losses due to the narrow slit width of $0''.7$ in our observations are corrected in this step, considering the seeing conditions. We assume our high-redshift target galaxies are point sources, as they are unresolved in our observations. Overall, we obtained 3σ detection limits of emission lines at $\sim 5 \times 10^{-18}$ erg s $^{-1}$ cm $^{-2}$ between sky-emission lines (with ~ 3.5 hr integration), and this is comparable to typical detection limits from previous MOSFIRE Y -band observations (e.g., Finkelstein et al. 2013; Song et al. 2016a; Jung et al. 2020).

3. Results

3.1. Emission-Line Search

We implemented an automated search scheme to capture plausible emission-line candidates consistently, similar to the method in Jung et al. (2020). We first collected emission-line candidates that were selected via our automated search on both 1D and 2D spectra by performing Gaussian line fitting on the 1D and SOURCE EXTRACTOR (Bertin & Arnouts 1996) runs on the 2D spectra. We required a 3σ detection threshold in both the 1D and 2D searches. Then, we manually inspected individual emission-line candidates to rule out (i) sky-emission residuals, (ii) spurious sources, and (iii) contaminants from nearby sources. We conservatively removed emission-line features that are found close to the edge of sky-emission lines. To rule out spurious sources, we inspected the 2D spectra to ensure that there are clear negative peaks shown at the expected locations, $\pm 2''.5$ apart from source positions, caused by the dither pattern of MOSFIRE. Additionally, we inspected the HST images to see if there are potential nearby contaminants whose emission lines could be captured at the same spatial locations of the MOSFIRE slits. Lastly, we performed tailored asymmetric (for the extended emission) or Gaussian (for the sharp/unresolved) emission-line fitting in reduced 1D spectra to calculate the line fluxes of emission-line candidates.

For emission-line-detected objects, we further checked their possibility of being low-redshift interlopers to ensure their nature as Ly α . First, we checked if multiple emission lines are found in the same object. These would originate from a combination of emission lines from low-redshift galaxies (e.g., [O III] $\lambda\lambda 4959, 5007$; H β ; [N II] $\lambda\lambda 6548, 6584$; H α). We manually inspected the wavelengths of the possible companion lines, and we find no evidence of multiple emission lines in our sample. Second, we checked the possible low-redshift solution of being an [O II] $\lambda\lambda 3727, 3729$ emitter which can mimic the Lyman-break feature with the Balmer break of low-redshift galaxies. If that is the case, the [O II] doublet should be resolved with the spectral resolution of Keck/MOSFIRE ($R = 3500$ or $\sim 3\text{\AA}$). However, none of our emission-line candidates display the doublet emission lines with a $\sim 7\text{--}8\text{\AA}$ separation (an expected peak separation of the [O II] doublet at $z \sim 1.7\text{--}1.8$).

We also compared the χ^2 values from best-fit SEDs between high-redshift (with Ly α) and low-redshift (with [O II]) solutions for Ly α -emission candidates as supplementary check, removing Ly α -emission candidates disfavored in SED fitting analysis. The best-fit model SEDs of the host galaxies are shown in Figure 4. Our SED fitting analysis presents that the high-redshift solutions with Ly α are preferred over the low-redshift solutions for our Ly α -detected galaxies in agreement with the photometric redshift PDFs.

From our emission-line search, we find eight galaxies with Ly α emission detected in the spectra ($\text{SNR} \geq 4$). The 1D

and 2D spectra of the detected emission lines are displayed in Figure 5. We caution that we are unable to completely rule out the chance of being low-redshift interlopers. The secondary lines that might have served to reject a high-redshift interpretation could be below the detection limit, particularly when coincident with a strong sky emission line. The strongly varying signal-to-noise can be seen in Figure 5. Nevertheless, based on our robust identification of emission lines and thorough diagnosis of low-redshift interlopers, we conclude that the detected emission lines are consistent with Ly α emission at $z > 7$.

3.2. $z > 7$ Ly α Emitters

3.2.1. Emission-Line Properties

Table 2 summarizes the properties of the detected Ly α -emission lines and their host galaxies. To measure emission-line properties, we performed 1D (asymmetric) Gaussian fitting to the reduced 1D spectra. The fiducial values were taken from the best-fit (asymmetric) Gaussian curves. To estimate the 1σ errors of the emission-line properties, we perform the same (asymmetric) Gaussian fitting to 1000 Monte Carlo realizations of the perturbed 1D spectra with corresponding error spectra. The spectroscopic redshifts are calculated from the peak wavelength of the best-fit Gaussian curves, and the line fluxes are obtained from the total fluxes under the Gaussian curves. The rest-frame equivalent width (EW) is estimated as:

$$EW = \frac{F_{\text{Ly}\alpha}}{f_{\text{cont}}(1 + z_{\text{Ly}\alpha})}, \quad (1)$$

where $F_{\text{Ly}\alpha}$ is the Ly α emission-line flux, and f_{cont} is the continuum flux density, derived by averaging rest-UV continuum of the best-fit SEDs within a 50\AA -wavelength window of the rest-frame $1230\text{--}1280\text{\AA}$.

In Figure 6, we show the Ly α EWs versus redshift (left), the rest-UV slope (middle), and M_{UV} (right). In the left panel, we highlight that five of our eight LAEs are clustered at $z \sim 7.7$ (red symbols) in close proximity to the known three LAEs at $z \sim 7.7$ presented in Tilvi et al. (2020). Although there is no significant trend seen with the rest-UV slope (β) in the middle panel, our LAEs are showing rest-UV slopes mostly bluer than $\beta \lesssim -1.5$. Interestingly, two of them emit the highest EW Ly α ($EW > 50\text{\AA}$) that are faintest in UV among our LAEs (in the right panel). We will discuss more details on the clustered LAEs in Section 4.

4. Extended Ionized Structure around Clustered LAEs at $z \sim 7.7$

4.1. Clustered LAEs at $z \sim 7.7$

The process of reionization is expected to be inhomogeneous as overdensity regions with clustered galaxies were to be ionized earlier than field areas (e.g., Finlator et al.

Table 2. Summary of New Ly α -Emission-Line and Host-Galaxy Properties^a

ID	R.A. (J2000.0)	Decl. (J2000.0)	$F_{\text{Ly}\alpha}$	SNR _{2D} ^a	EW _{Lyα} ^b	$z_{\text{Ly}\alpha}$	M_{UV}	β^c
	degree	degree	(10^{-17} erg s ⁻¹ cm ⁻²)		(\AA)			
(1)	(2)	(3)	(4)	(5)	(6)	(7)	(8)	(9)
z7.13433	214.85083	52.77666	1.53 \pm 0.37	4.7	22.2 $^{+8.6}_{-7.0}$	7.4784 \pm 0.0019	-22.1	-1.52 $^{+0.24}_{-0.22}$
z7.20237	215.10658	52.97582	0.46 \pm 0.09	5.9	17.1 $^{+8.6}_{-5.7}$	7.6228 \pm 0.0003	-21.1	-2.23 $^{+0.52}_{-0.49}$
z7.8626	215.11446	52.95123	1.06 \pm 0.09	10.3	49.4 $^{+17.5}_{-11.7}$	7.6682 \pm 0.0002	-21.0	-1.67 $^{+0.44}_{-0.61}$
z8.13573	215.15088	52.98957	1.23 \pm 0.18	9.1	69.1 $^{+29.8}_{-19.9}$	7.7482 \pm 0.0009	-20.7	-1.80 $^{+0.47}_{-0.53}$
z7.27591	215.13288	53.04786	0.49 \pm 0.17	5.3	19.1 $^{+9.0}_{-7.6}$	7.7496 \pm 0.0007	-20.8	-2.80 $^{+0.39}_{-0.25}$
z7.30645	215.09504	53.01421	0.56 \pm 0.17	4.0	8.7 $^{+4.3}_{-3.4}$	7.7496 \pm 0.0009	-22.1	-2.18 $^{+0.28}_{-0.33}$
z8.32350	214.99903	52.94197	1.01 \pm 0.18	4.6	17.7 $^{+8.6}_{-5.7}$	7.7759 \pm 0.0012	-21.9	-1.98 $^{+0.37}_{-0.55}$
z8.19326	215.11962	52.98284	1.55 \pm 0.41	4.0	151.0 $^{+125.4}_{-66.2}$	7.7832 \pm 0.0035	-20.1	-1.56 $^{+0.37}_{-0.62}$

NOTE—Columns: (1) Object ID, (2) Right ascension, (3) Declination, (4) Ly α emission line flux, (5) Emission-line detection significance, (6) Rest-frame equivalent width of Ly α emission line, (7) spectroscopic redshift based on Ly α emission line, (8) galaxy UV magnitude estimated from the averaged flux over a 1450 – 1550 \AA bandpass from the best-fit galaxy SED model, (9) Rest-UV continuum slope.

^aDetection significance measured from SOURCE EXTRACTOR runs on 2D spectra.

^bListed uncertainties account for the UV continuum measurement errors from SED fitting.

^cThe power-law slope of the rest-frame UV continuum, measured from the best-fit SEDs.

2009; Mesinger et al. 2015; Katz et al. 2019). The currently most accessible tool to probe ionized structures in the middle of reionization is to search for Ly α emission from the reionization-era galaxies. A recent effort to spectroscopic search for Ly α resulted in the discoveries of clustered LAEs in the middle/late phase of reionization at $z \sim 7 - 8$ (e.g., Zheng et al. 2017; Castellano et al. 2018; Tilvi et al. 2020; Jung et al. 2020; Endsley et al. 2021a). Particularly, the EGS field has a couple of known clustered structures with LAEs at $z \gtrsim 7.5$ (Zitrin et al. 2015; Oesch et al. 2015; Roberts-Borsani et al. 2016; Tilvi et al. 2020; Larson et al. 2022), and their additional membership candidates are discussed based on photometric selection (Leonova et al. 2022). Our MOS-FIRE Y-band program detected Ly α emission from eight sources, and five of them are potentially associated with the known $z \sim 7.7$ LAE cluster (Tilvi et al. 2020)⁵. This demonstrates a possible extension of the LAE structure with up to eight LAEs at $z \sim 7.7$. This is currently the largest measured LAE cluster system in this early Universe at $z > 7$. We summarize the $z \sim 7.7$ LAEs in Table 3.

4.2. Extended Ionized Structure

With the discovery of the clustered LAEs at $z \sim 7.7$, we calculate 3-dimensional (3D) separations of individual $z \sim 7.7$ LAEs from the brightest (and potentially central)

galaxy (z8.5). The left panel of Figure 7 shows the distribution of our $z \sim 7.7$ LAEs (green) in addition to the three $z \sim 7.7$ LAEs that were previously discovered (white; Oesch et al. 2015; Roberts-Borsani et al. 2016; Tilvi et al. 2020). The estimated 3D physical distances from z8.5 are listed in parentheses, ranging from 0.7pMpc at the nearest to 2.5pMpc at the farthest.

The crowd of ionizing sources could create the extended ionized structure beyond a ~ 1 pMpc scale of individual ionized bubbles and eventually enhance Ly α transmission in the IGM. To examine whether these clustered objects are situated in a connected ionized structure, we estimated the ionized bubble sizes which could be created by individual LAEs. Following Tilvi et al. (2020) and Jung et al. (2020), we used the relation between Ly α luminosities and ionized bubble sizes, predicted in the theoretical models from Yajima et al. (2018). Briefly, Yajima et al. (2018) model LAEs and the ionized bubble sizes based on individual halo merger trees using star formation history which is modeled to provide a reionization history consistent with the Planck observations (Planck Collaboration et al. 2016). Based on the Yajima et al. (2018) models, we used the measured Ly α luminosities to derive the predicted sizes of individual ionized bubbles around LAEs. The estimated ionized bubble sizes are ranging from ~ 0.7 to 1.0 pMpc, as listed in Table 3. As the models in Yajima et al. (2018) predict the growth of isolated ionized bubbles around LAEs, it does not consider the additional expansion due to the overlapping ionized bubbles. Thus, the derived ionized bubble sizes may indicate the lower limits of ionized

⁵ Ly α from the brightest galaxy (z8.5) was first detected in Oesch et al. (2015) and Roberts-Borsani et al. (2016), and its CIII] emission was detected in Stark et al. (2017).

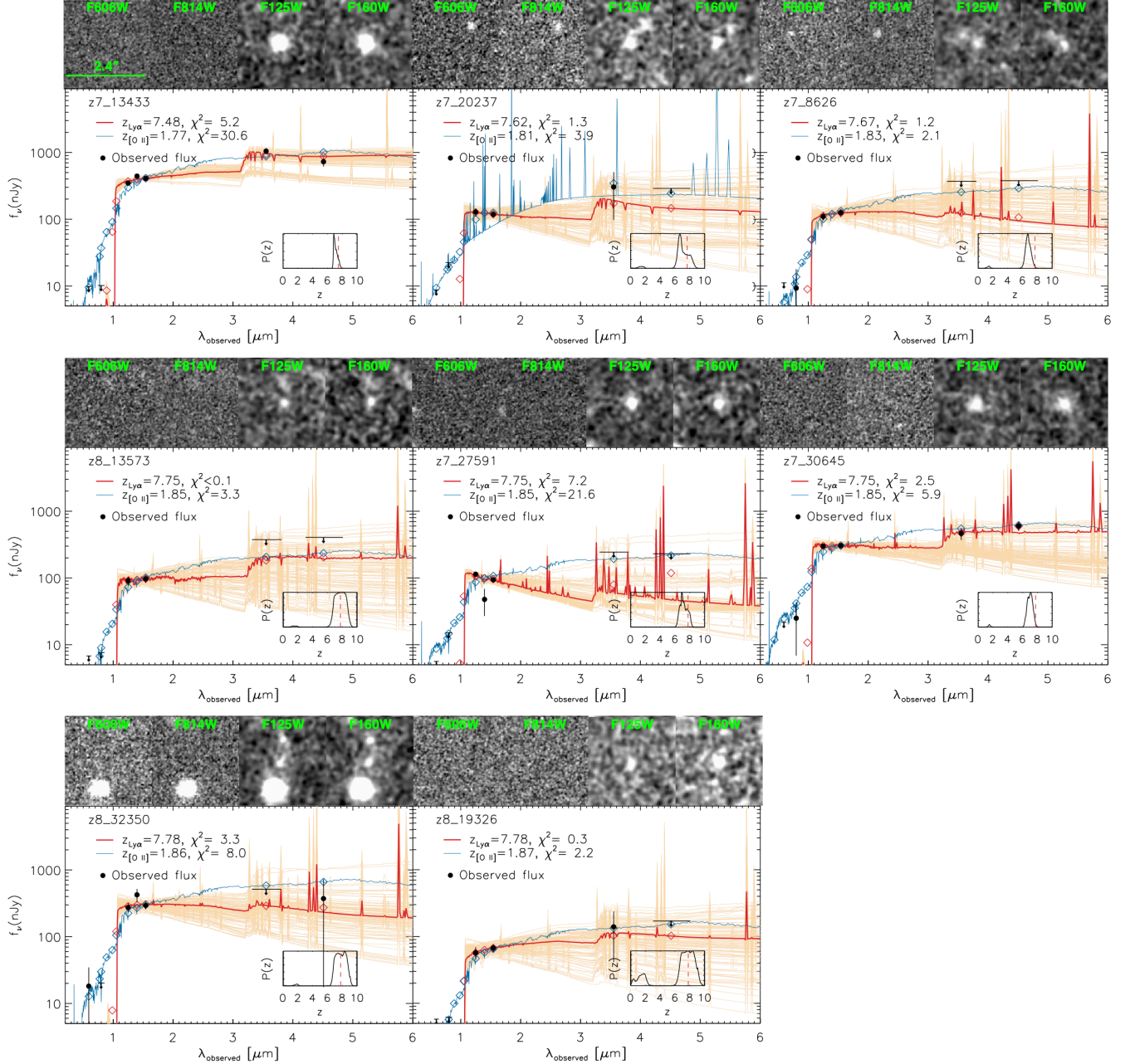


Figure 4. The best-fit model SEDs of our $z > 7$ LAEs. The best-fit model SEDs of high-redshift solutions (Ly α) are shown as red curves, and the 100 random draws are displayed as thin lines in each panel. We also show the best-fit SEDs from low-redshift solutions of [O II] as blue curves for comparison. The photometric data in HST and *Spitzer*/IRAC filters are shown as black symbols, and the downward arrows represent 1σ upper limits. The inset figures show the photometric redshift PDFs with spectroscopic redshifts from Ly α as dashed vertical lines. The small HST cutouts of individual objects in the V_{606} , I_{814} , J_{125} , and H_{160} filters are on top of each panel, which highlight strong Lyman-break between I_{814} and J_{125} images.

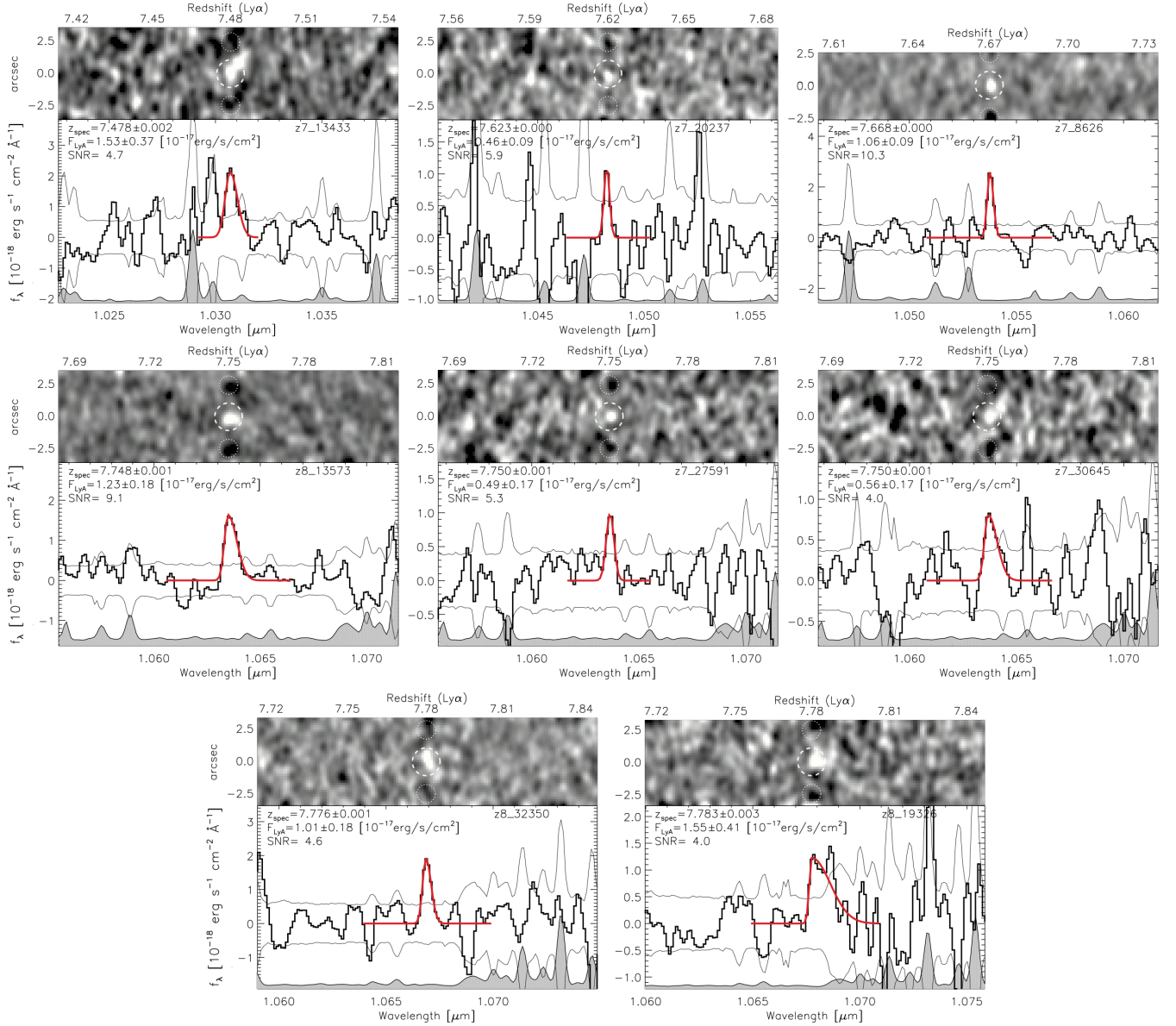


Figure 5. MOSFIRE spectra of the detected Ly α emission lines: 2D on top and 1D at the bottom in each panel. In each panel, 1D and 2D spectra are centered at the detected emission line. At the bottom, the solid black lines are the 1D signals with 1σ upper and lower bounds shown as thin grey curves. Sky-emission regions are shown as the shaded curves at the bottom of each plot. In 2D spectra, red circles denote the emission lines, and the negative traces caused by a dither pattern are marked with white circles. The red curves in 1D represent the best-fit asymmetric Gaussian curves. All emission lines are found within the expected spatial locations in the 2D spectra (within ± 3 pixels in the y-axis), and two negative features, caused by our dither pattern, are shown at around ± 2.5 from the detected emission lines.

bubble sizes around LAEs; a much larger ionized structure could be created by the overlaps of multiple ionized bubbles around these LAEs. Such an extended ionized structure may promote Ly α escape from galaxies (e.g., Mason & Gronke 2020; Park et al. 2021; Qin et al. 2021; Smith et al. 2021), resulting in enhanced Ly α detection rate in our observations at this redshift.

4.3. Enhanced Ly α Detection Rate at $z \sim 7.7$

The detectability of Ly α emission in targeted spectroscopic observations is affected by target selection functions (which considers photometric redshift measurement PDFs and galaxy M_{UV} distribution) and detection limits (depending on e.g., observing conditions and the presence of sky-emission lines) in addition to the Ly α IGM transmission particularly during the epoch of reionization. Thus, this makes it complicated to interpret a Ly α detection rate at its face value.

Instead, we performed Ly α EW distribution modeling to estimate the expected number of Ly α detections in our ob-

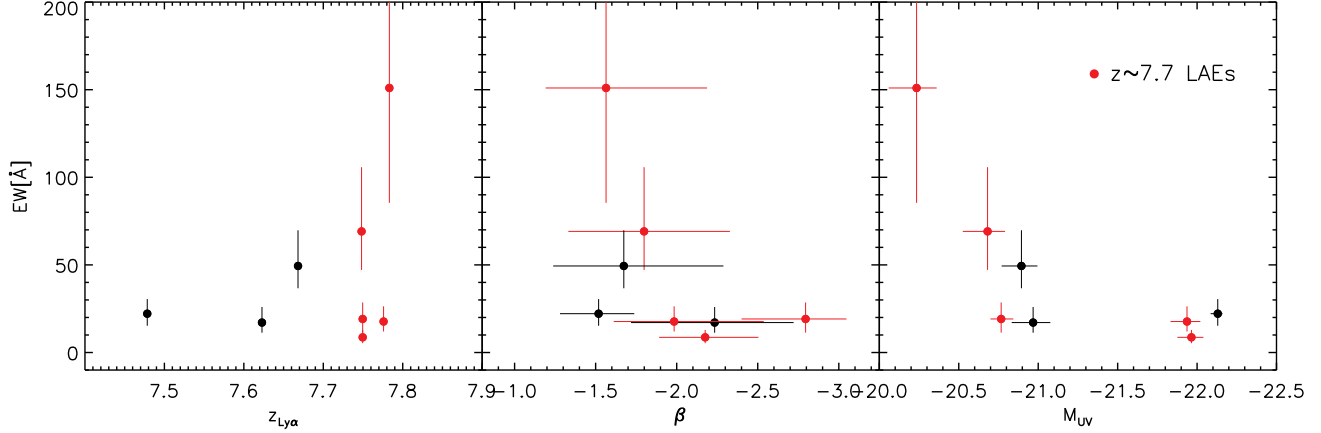


Figure 6. Rest-frame Ly α EWs versus redshift (left), the rest-UV continuum slope (middle), and M_{UV} (right). The $z \sim 7.7$ LAEs are symbolized with red circles. Interestingly, two of the $z \sim 7.7$ LAEs, which are the faintest in UV among our LAEs, emit the highest EW Ly α emission lines ($EW > 50\text{\AA}$) as shown in the right panel.

Table 3. Summary of Ly α Emitters at the $z \sim 7.7$ Overdensity

ID	R.A. (J2000.0)	Decl. (J2000.0)	$z_{Ly\alpha}$	$L_{Ly\alpha}$	H II radii	Δ_{3D} from z8.5	M_{UV}
	degree	degree		(10^{43} erg s $^{-1}$)	(pMpc)	(pMpc)	
(1)	(2)	(3)	(4)	(5)	(6)	(7)	(8)
New Lyα Emitters in this work							
z8.13573	215.15088	52.98957	7.7482 ± 0.0009	0.93 ± 0.14	0.93	0.7	-20.7
z7.27591	215.13288	53.04786	7.7496 ± 0.0007	0.37 ± 0.13	0.68	1.1	-20.8
z7.30645	215.09504	53.01421	7.7496 ± 0.0009	0.42 ± 0.13	0.71	0.9	-22.1
z8.32350	214.99903	52.94197	7.7759 ± 0.0012	0.77 ± 0.14	0.87	2.5	-21.9
z8.19326	215.11962	52.98284	7.7832 ± 0.0035	1.18 ± 0.31	1.01	1.9	-20.1
Lyα Emitters in Tilvi et al. (2020)^a							
z8.5	215.14530	53.00423	7.728	1.2 ± 0.1	1.02	-	-22.3 ^b
z8.4	215.14654	52.99461	7.748	0.4 ± 0.1	0.69	0.7	>-20.3
z8.SM	215.14873	53.00259	7.767	0.2 ± 0.1	0.55	1.4	>-20.3

NOTE—Columns: (1) Object ID, (2) Right ascension, (3) Declination, (4) spectroscopic redshift based on Ly α emission line, (5) Ly α emission luminosity, (6) radii of ionized H II bubble around LAEs based on the relation between Ly α luminosities and the bubble sizes from the Yajima et al. (2018) model (see more discussion in Section 4.2), (7) Physical 3D separation from z8.5, (8) galaxy UV magnitude estimated from the averaged flux over a 1450 – 1550 \AA bandpass from the best-fit galaxy SED model.

^a The listed values are taken from Tilvi et al. (2020).

^b M_{UV} for this object is not given in Tilvi et al. (2020), thus we calculate it from our SED fitting analysis as same as done for other galaxies.

servations, which also consider target selection as well as observational conditions. Following Jung et al. (2020), in our Ly α EW modeling, we assume the Ly α EW distribution in its exponential functional form, $dN/dEW \propto \exp(-EW)/W_0$, characterized with an e -folding scale (W_0). We populate mock Ly α emission lines for spectroscopic targets with (i) EW values that are randomly taken from the assumed EW distributions and (ii) wavelength locations, also randomly chosen based on galaxy photometric redshift PDFs. We cal-

culate the expected detection rates above the detection limits of these simulated Ly α emission lines. To sum up, we quantify the Ly α detectability into the expected number of detections above detection limits as a function of W_0 via our EW modeling.

In the right panel of Figure 7, we compare the actual Ly α detection to what is estimated in our EW modeling. The figure shows the number of Ly α detection above detection limits per unit volume, a 1cMpc-thick slice in the line-of-sight

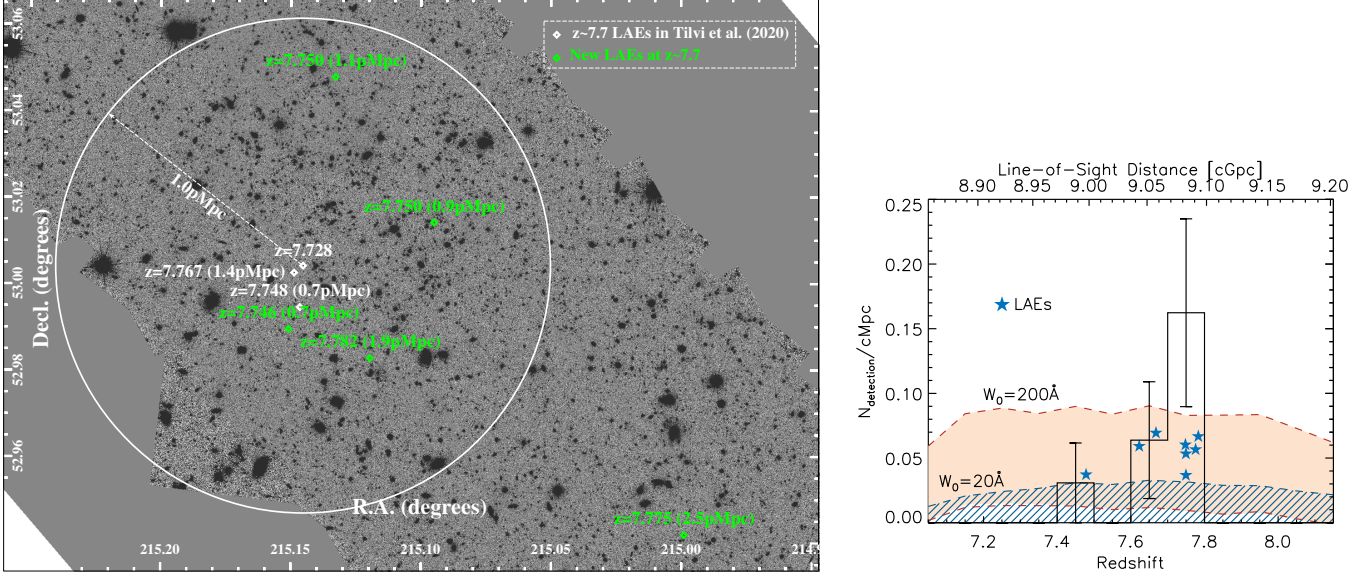


Figure 7. (Left) Spatial distribution of $z \sim 7.7$ LAEs in the CANDELS EGS field, displayed on the HST H -band image. Three $z \sim 7.7$ LAEs reported in [Tilvi et al. \(2020\)](#) are shown as white diamond points, and the new $z \sim 7.7$ LAEs discovered in this work are marked as green symbols. The white circle represents a 1pMpc-radius ionized bubble, which is estimated to be produced by the brightest galaxy ($z_{8.5}$) in [Tilvi et al. \(2020\)](#), and the 3D spatial separations of new $z \sim 7.7$ LAEs from $z_{8.5}$ are shown in parentheses. Seven $z \sim 7.7$ LAEs are clustered within $\lesssim 2$ pMpc, and an additional LAE is at a 2.5pMpc distance. As the estimation of ionized bubble size is typically based on a single source, an extended (> 2.5 pMpc) ionized structure could be created by overlapping ionized bubbles. (Right) LAE density as a function of redshift. The plot shows the number of Ly α detections above observational detection limits per unit volume, a 1cMpc-thick slice in the line-of-sight (LOS) direction. The actual detections from our observations are shown as histograms with the Poissonian errors in individual bins. The blue star symbols denote spectroscopic redshifts of the LAEs, that are arbitrarily distributed along the y-axis to avoid overlaps. The shaded regions represent the 1σ ranges of the expected numbers of Ly α detections from our EW distribution modeling. The case of the high Ly α EW distribution with $W_0 = 200\text{\AA}$ is shown as a red-shaded area, and the low Ly α EW case of $W_0 = 20\text{\AA}$ is displayed with a diagonal-pattern filled region. This plot reveals a clear spike at $z \sim 7.7$. The $z \sim 7.7$ spike is more comparable to the extreme case of the high Ly α EW distribution whereas the low Ly α EW case explains well the low/non-detections of Ly α at other redshift ranges.

(LOS) direction in the sky area covered in our observations. We present the 1σ range of the expected Ly α detections for the high and low Ly α EW cases with $W_0 = 200\text{\AA}$ and 20\AA , respectively. The choice of $W_0 = 200\text{\AA}$ represents the distribution of extremely large EW Ly α emission lines whereas the low Ly α EW case of $W_0 = 20\text{\AA}$ is comparable to the statistical measurement of W_0 from $M_{UV} < -20$ galaxies in this redshift ([Jung et al. 2022](#)). In the figure, the redshift distribution of our actual Ly α detections are shown as the blue star symbols, and the black histogram shows the estimated detection number density per unit volume. The spike of our actual Ly α detection at $z \sim 7.7$ exceeds the expectation of the extreme case of the high Ly α EW distribution ($W_0 = 200\text{\AA}$ red shades) whereas non/rare detections of Ly α at other redshift ranges are more consistent with the low Ly α EW case ($W_0 = 20\text{\AA}$). Even without the three known LAEs of [Tilvi et al. \(2020\)](#), our Ly α -detection-rate analysis demonstrates that we observe significantly stronger Ly α from the clustered galaxies compared to that from the rest of the galaxies.

4.4. Boosted IGM Transmission of Ly α from Galaxies in the Rear Side of Ionized Bubbles

As discussed above, Ly α transmission can be enhanced in an extended ionization structure formed by clustered galaxies because the Ly α transmissivity increases with the distance between the source and the boundary of the ionized region (e.g., [Dijkstra 2014](#)). It is remarkable that the brightest member ($z_{8.5}$) of the clustered LAEs has the lowest redshift in the cluster indicating that it is likely located in front of all the other LAEs toward the observer (see the right panel of [Figure 8](#)). That is, we may be witnessing a bright galaxy boosting the Ly α visibility preferentially on its rear side.

The left panel of [Figure 8](#) illustrates how Ly α transmissivity can be boosted in the rear side of a bright galaxy. The bright galaxy may be located at the center of the local ionized bubble. The ionized bubble opens a wavelength window on the red side of Ly α where photons can avoid being resonantly scattered by the neutral IGM. Ly α photons from galaxies on the rear side experience a larger cosmological redshift before reaching the neutral region and have a better chance of transmitting through the window. Indeed, a simulation study by [Park et al. \(2021\)](#) reported that fainter galaxies tend to have a larger variation in Ly α transmission as their transmissivity

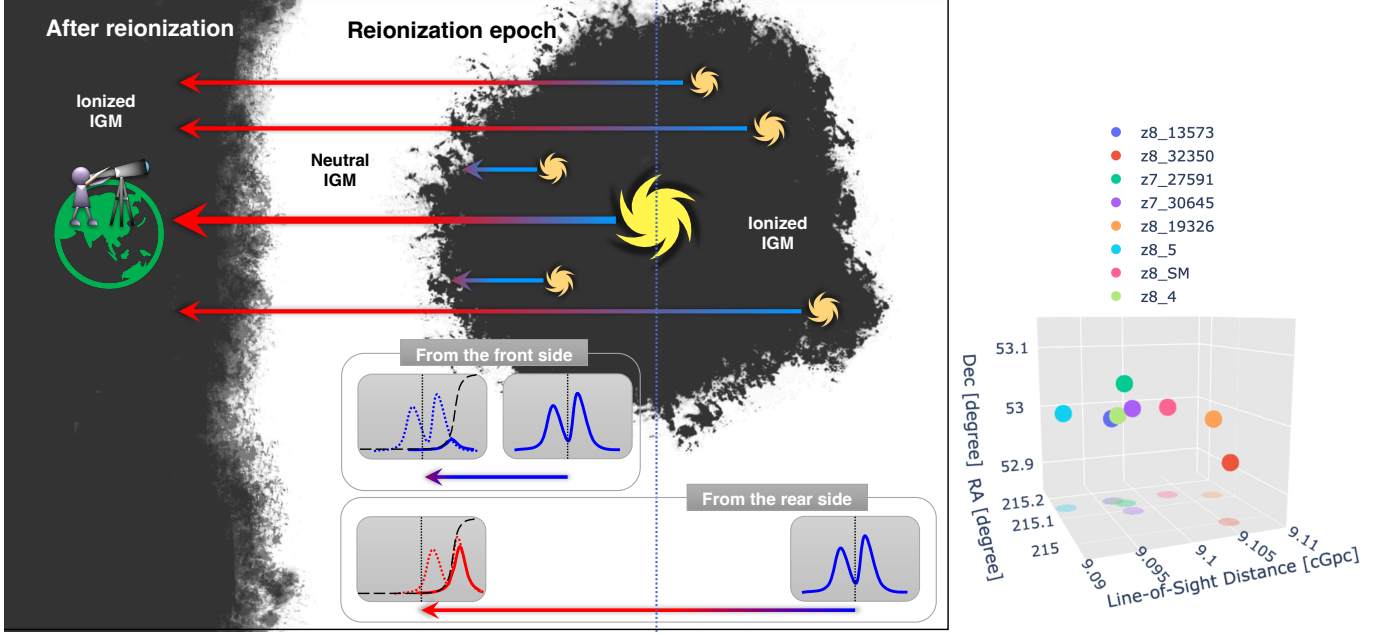


Figure 8. (Left) Cartoon depicting boosted $\text{Ly}\alpha$ visibility through the IGM from galaxies in the rear side of ionized bubbles. The inset figures at the bottom illustrate the $\text{Ly}\alpha$ line shift in the rest frame of the neutral IGM. The black long-dashed lines in the left inset panels show the wavelength-dependent IGM transmission. $\text{Ly}\alpha$ from the rear-side galaxies is significantly shifted to red from the central velocity while the line shift is much less for $\text{Ly}\alpha$ from the front-side galaxies. This results in relatively boosted IGM transmission to $\text{Ly}\alpha$ from galaxies in the rear side of ionized bubbles. (Right) Spatial distribution of the clustered LAEs, including three LAEs of Tilvi et al. (2020): $z8_5$, $z8_4$, and $z8_SM$. The faint symbols represent the projections in the bottom plane. The brightest galaxy ($z8_5$) is shown as the cyan point, which is placed in front of the other LAEs in the LOS direction.

sensitively depends on where they are located with respect to their brighter neighbors.

A peculiar motion of galaxies can contribute to the line shift as well. However, the redshift range of these clustered LAEs corresponds to $\gtrsim 1000 \text{ km s}^{-1}$ in velocity, which is too large to be explained by the gravitational dynamics of galaxies alone. In theoretical studies, galaxies that are similar to $z8_5$ in UV magnitude have their total masses around $\sim 10^{12} M_{\odot}$ (e.g., Ocvirk et al. 2020). The gravitational infall velocity of such a galaxy peaks at $\sim 250\text{--}300 \text{ km s}^{-1}$ near the virial radius ($\sim 0.04 \text{ pMpc}$ at $z = 7.7$) and decreases as $r^{-0.5}$ with increasing distance to the galaxy (r). As the clustered LAEs spread out over a $\gtrsim 1 \text{ pMpc}$ distance, we conclude that the LAEs observed here are far from forming a dynamically relaxed system in this early Universe.

4.5. Comparison with UV-faint Galaxy Observations

Recent surveys have produced a higher yield of $\text{Ly}\alpha$ detections from UV-luminous ($M_{\text{UV}} \lesssim -20$) galaxies than earlier attempts (e.g., Castellano et al. 2018; Jung et al. 2019, 2020, and in this work). In particular, spectroscopic observations of luminous sources with IRAC color excess, which reflects intense $[\text{O III}]+\text{H}\beta$ emission, delivered a much higher $\text{Ly}\alpha$ detection rate (e.g., Oesch et al. 2015; Zitrin et al. 2015; Roberts-Borsani et al. 2016; Stark et al. 2017; Endsley et al. 2021b; Laporte et al. 2021). In contrast, $\text{Ly}\alpha$ has

rarely been detected in follow-up spectroscopic observations of UV-faint ($M_{\text{UV}} \gtrsim -20$) galaxies (Hoag et al. 2019; Mason et al. 2019). Moreover, the unusually high detection rate of $\text{Ly}\alpha$ from galaxies with the IRAC excess is again somewhat diminished when it comes to targeting faint galaxies (Roberts-Borsani et al. 2022b). Additionally, $\text{Ly}\alpha$ emission has not been detected in the recent JWST NIRSpec observations which targeted UV-faint galaxies (Roberts-Borsani et al. 2022a; Williams et al. 2022; Morishita et al. 2022).

This notable difference in a $\text{Ly}\alpha$ detection rate between UV-luminous and UV-faint populations could be understandable in the sense that an inhomogeneous nature of reionization suggests an earlier process of reionization around overdense regions where bright galaxies are preferentially located (e.g., Finlator et al. 2009; Katz et al. 2019; Ocvirk et al. 2021; Kannan et al. 2022). Although Morishita et al. (2022) report non-detection of $\text{Ly}\alpha$ even from clustered galaxies, those galaxies are less luminous (with $M_{\text{UV}} \gtrsim -20$) than those studied here. Thus they may not create ionized regions large enough to allow the escape of $\text{Ly}\alpha$.

5. Summary and Discussion

We present our analysis of Keck/MOSFIRE Y -band spectroscopic observations for $\text{Ly}\alpha$ at $61.7.0 < z < 8.2$ from 61 high-redshift candidate galaxies in the CANDELS EGS field, covering a total effective sky area of $\sim 10' \times 10'$. Most of our

spectroscopic targets are relatively UV-bright ($M_{UV} \lesssim -20$). Our findings are summarized as follows.

1. We provide spectroscopic confirmations of Ly α ($>4\sigma$) from eight galaxies at $z > 7$. This includes five potential members of the $z \sim 7.7$ LAE cluster. Interestingly, two of them emit the highest EW Ly α emission lines (EW $> 50\text{\AA}$) that are the faintest in UV among our LAEs.
2. The five $z \sim 7.7$ LAEs from our observations are potentially associated with the known $z \sim 7.7$ LAEs (Tilvi et al. 2020), forming eight clustered LAEs at $z \sim 7.7$. This is currently the largest measured LAE cluster system in this early Universe at $z > 7$.
3. From our Ly α EW modeling, we estimated expected Ly α detection rates per unit volume in the line-of-sight (LOS) direction (or a redshift bin) depending on the choice of Ly α EW distribution. It suggests significantly stronger Ly α from the clustered $z \sim 7.7$ LAEs, compared to the rest of our targets.
4. We conclude that the clustered LAEs are likely to form an extended ionized structure around them based on the estimate of ionized bubble sizes around individual LAEs. The existence of such an extended ionized structure may allow the easier escape of Ly α from galaxies inside. This is aligned with the enhanced detection rate of Ly α at $z \sim 7.7$.
5. We notice that the brightest object (z8_5) in the $z \sim 7.7$ LAE cluster is located at slightly lower (Ly α) redshift than the other $z \sim 7.7$ LAEs. This may indicate that we are witnessing the boosted IGM transmission of Ly α from galaxies that are situated on the rear side of an ionized area.
6. Our observations, which targeted UV-bright ($M_{UV} \lesssim -20$) candidate galaxies, yield a relatively high Ly α detection rate. This is in contrast to non/rare detection of Ly α reported in recent spectroscopic searches on UV-faint galaxies. This notable difference in a Ly α detection rate between UV-bright and -faint galaxies suggests an inhomogeneous nature of reionization in which reionization proceeds faster in overdense regions where bright galaxies are preferentially populated.

Ly α is a major observational probe to trace the evolution of reionization. The presence of the clustered Ly α emitters reported in this work indicates that we are witnessing ionized regions in the IGM whereas the nondetections of Ly α from other sources reflect the neutral IGM. This is consistent with the general picture of reionization on the inhomogeneity in

reionization. Particularly, the LOS distribution of the $z \sim 7.7$ cluster LAEs, in which the brightest galaxy is found in front of the others, suggests that the detailed analysis of Ly α observations on the IGM transmission can hint at outlining the scope of ionized regions around reionization-era galaxies as well as investigating how galaxies are distributed inside.

We caution that interpreting these results from Ly α observations remains challenging. This is mainly because current Ly α studies generally rely on the photometric selection of galaxies when their spectroscopic confirmations are not available, which inevitably includes some portion of low-redshift interloper galaxies. In addition, the lack of direct measurements of Ly α velocity offsets causes significant uncertainties in estimating the Ly α transmission from observations (e.g., Mason et al. 2018; Hoag et al. 2019; Jung et al. 2020, 2022). Additionally, the size distribution of ionized bubbles also plays an important role in determining Ly α transmission at a fixed IGM neutral fraction (e.g., Matthee et al. 2018; Mason & Gronke 2020; Park et al. 2021; Qin et al. 2021; Smith et al. 2021). These factors eventually compound the uncertainty of the final measurement of the neutral fraction of the IGM from Ly α observations.

JWST observations, however, can place critical constraints on these uncertainties and improve the use of Ly α as a probe of reionization. Specifically, even in the darkness of Ly α , JWST can confirm the redshifts of numerous galaxies with non-Ly α emission lines or the Lyman-alpha break. Also, Ly α velocity offsets can be measured directly from non-resonant emission lines. Additionally, improved estimates of the ionizing photon production rate are possible via the use of nebular emission lines and/or better-constrained SED modeling (e.g., Williams et al. 2022; Robertson et al. 2022), which constrains the size of ionized bubbles around galaxies. In the new era of JWST, Ly α observations will eventually allow us to place strong constraints on the IGM neutral fraction during the epoch of reionization.

I.J. acknowledges support from NASA under award number 80GSFC21M0002. TAH is supported by an appointment to the NASA Postdoctoral Program (NPP) at NASA Goddard Space Flight Center, administered by Oak Ridge Associated Universities under contract with NASA. This work was supported by a NASA Keck PI Data Award, administered by the NASA Exoplanet Science Institute. Data presented herein were obtained at the W. M. Keck Observatory from telescope time allocated to the National Aeronautics and Space Administration through the agency's scientific partnership with the California Institute of Technology and the University of California. The Observatory was made possible by the generous financial support of the W. M. Keck Foundation. The authors wish to recognize and acknowledge the very significant cultural role and reverence that the summit of Maunakea has

always had within the indigenous Hawaiian community. We are most fortunate to have the opportunity to conduct observations from this mountain.

Appendix

A. Spectroscopic Targets for Ly α

We list our spectroscopic targets in Table A in order of decreasing photometric redshift, which includes the 3σ rest-EW upper limits of Ly α for nondetection objects in the last column.

Table 4. Summary of Spectroscopic Targets

ID	R.A. (J2000.0)	Decl. (J2000.0)	J_{125}	M_{UV}^a	z_{phot}^b	z_{spec}^c	EW _{Lyα} ^d (Å)
z8_7364	215.035610	52.892210	25.6	-21.8	$8.14^{+0.56}_{-0.66}$	-	<35.7
z8_62818	214.793960	52.841540	26.0	-21.1	$8.04^{+0.27}_{-0.29}$	-	<53.9
z8_14498	214.943550	52.845650	26.6	-20.6	$7.80^{+0.72}_{-0.83}$	-	<92.5
z8_70475	215.103630	53.043030	26.5	-20.7	$7.79^{+0.81}_{-1.48}$	-	<57.2
z8_19326	215.119620	52.982840	27.0	-20.2	$7.79^{+0.75}_{-5.68}$	7.783	$151.0^{+125.4}_{-66.2}$
z8_32350	214.999030	52.941970	25.3	-21.9	$7.82^{+0.72}_{-0.77}$	7.776	$17.7^{+8.6}_{-5.7}$
z7_30645	215.095040	53.014210	25.2	-22.0	$7.00^{+0.36}_{-0.40}$	7.750	$8.7^{+4.3}_{-3.4}$
z7_27591	215.132880	53.047860	26.3	-20.8	$7.18^{+0.58}_{-0.51}$	7.750	$19.1^{+9.0}_{-7.6}$
z8_13573	215.150880	52.989570	26.5	-20.7	$7.74^{+0.72}_{-0.76}$	7.748	$69.1^{+29.8}_{-19.9}$
z7_8626	215.114460	52.951230	26.3	-20.9	$6.76^{+0.36}_{-0.40}$	7.668	$49.4^{+17.5}_{-11.7}$
z8_57340	215.100080	53.072100	26.2	-21.0	$7.66^{+0.72}_{-1.04}$	-	<36.6
z8_35089	215.080330	52.993230	24.8	-22.4	$7.65^{+0.59}_{-0.60}$	-	<11.2
z7_20237	215.106580	52.975820	26.1	-21.0	$7.13^{+0.81}_{-0.72}$	7.623	$17.1^{+8.6}_{-5.7}$
z8_48797	215.136960	53.001580	26.6	-20.4	$7.62^{+0.57}_{-0.63}$	-	<86.8
z8_47409	214.882250	52.824670	26.8	-20.4	$7.61^{+0.77}_{-1.35}$	-	<93.9
z8_55956	214.737210	52.818380	26.6	-20.5	$7.60^{+0.73}_{-1.28}$	-	<78.3
z8_52358	214.728630	52.820880	26.5	-20.6	$7.59^{+0.79}_{-5.31}$	-	<93.9
z8_67892	214.880950	52.891200	26.4	-20.7	$7.56^{+0.64}_{-5.49}$	-	<93.7
z8_21868	214.813040	52.834230	26.6	-20.4	$7.53^{+0.53}_{-1.01}$	-	<84.7
z7_64424	215.131670	53.076920	26.1	-21.0	$7.52^{+0.51}_{-0.40}$	-	<30.7
z7_13433	214.850830	52.776660	25.0	-22.1	$7.11^{+0.28}_{-0.26}$	7.478	$22.2^{+8.6}_{-7.0}$
z7_31938	215.130040	53.035510	26.3	-20.8	$7.46^{+0.55}_{-0.54}$	-	<33.6
z7_61615	214.995500	52.987580	26.5	-20.6	$7.44^{+0.74}_{-1.03}$	-	<67.7
z7_63317	214.862990	52.889430	25.9	-21.1	$7.42^{+0.62}_{-0.67}$	-	<49.0
z7_66460	214.990460	52.971990	26.0	-21.0	$7.37^{+0.63}_{-0.54}$	-	<33.0
z7_17991	215.077870	52.950110	27.1	-19.9	$7.36^{+0.58}_{-0.67}$	-	<121.5
z7_61983	215.132630	53.084080	25.9	-21.2	$7.36^{+0.37}_{-0.31}$	-	<22.8
z7_12730	215.138580	52.978710	26.8	-20.3	$7.35^{+0.81}_{-5.72}$	-	<85.9
z7_22848	215.115790	53.045690	25.9	-21.0	$7.33^{+0.61}_{-0.80}$	-	<25.2
z7_68268	215.009710	52.981390	24.9	-22.2	$7.30^{+0.61}_{-0.78}$	-	<15.1
z7_22554	215.132580	53.058960	27.4	-19.6	$7.29^{+0.89}_{-1.34}$	-	<108.3
z6_39031 ^e	215.144960	53.029710	25.5	-21.4	$7.64^{+0.47}_{-0.45}$	-	-
z7_16064	215.091040	52.954280	26.8	-20.2	$7.25^{+0.60}_{-0.80}$	-	<92.6
z7_36800	214.797330	52.788880	26.8	-20.1	$7.25^{+0.80}_{-0.95}$	-	<118.5
z7_33661	215.079120	52.995750	26.9	-19.9	$7.25^{+0.70}_{-0.60}$	-	<153.4

Table 4 continued

Table 4 (continued)

ID	R.A. (J2000.0)	Decl. (J2000.0)	J_{125}	M_{UV}^a	z_{phot}^b	z_{spec}^c	$EW_{Ly\alpha}^d$ (Å)
z7_39792	214.941730	52.884560	26.3	-20.7	$7.23^{+0.51}_{-4.84}$	-	<111.5
z7_27932	214.859170	52.853590	26.2	-20.7	$7.14^{+0.66}_{-5.74}$	-	<51.9
z7_69794	215.077540	53.026070	26.0	-21.2	$7.11^{+0.32}_{-0.42}$	-	<25.7
z7_12383	214.891540	52.803070	25.9	-21.1	$7.11^{+0.74}_{-5.33}$	-	<47.1
z7_34392	214.946710	52.900520	26.6	-20.5	$7.10^{+0.39}_{-0.44}$	-	<105.4
z7_60238	215.103540	53.067080	27.0	-20.0	$6.97^{+0.81}_{-1.28}$	-	<115.9
z7_48468	215.068000	52.953770	25.9	-21.1	$6.96^{+0.29}_{-0.30}$	-	<37.2
z7_64385	214.805040	52.845870	27.0	-19.6	$6.92^{+0.66}_{-5.23}$	-	<229.5
z7_39204	214.828420	52.810830	25.0	-22.1	$6.91^{+0.28}_{-0.31}$	-	<14.5
z6_40811	214.855170	52.820750	26.0	-21.0	$6.76^{+0.09}_{-5.68}$	-	<48.3
z6_10540	214.979940	52.861100	25.5	-21.3	$6.68^{+0.54}_{-0.44}$	-	<43.8
z7_18441	215.032080	52.918970	26.5	-20.2	$6.66^{+0.49}_{-0.73}$	-	<109.6
z7_15372	214.987940	52.879440	25.1	-21.8	$6.54^{+0.12}_{-0.12}$	-	<22.5
z6_20474	215.005970	52.905310	25.3	-21.6	$6.49^{+0.09}_{-5.04}$	-	<23.7
z6_47325	215.026580	52.927140	26.1	-20.6	$6.40^{+0.30}_{-5.02}$	-	<43.5
z6_12266	214.879170	52.793910	25.3	-21.5	$6.39^{+0.18}_{-0.33}$	-	<20.5
z6_23620	215.162130	53.077280	25.6	-21.2	$6.26^{+0.13}_{-4.69}$	-	<21.1
z6_24994	215.006790	52.965040	25.5	-21.3	$6.22^{+0.12}_{-0.13}$	-	<21.4
z6_69545	214.984000	52.960450	25.2	-21.4	$6.12^{+0.30}_{-0.44}$	-	<25.1
z6_12561	215.007900	52.886100	25.7	-21.0	$6.11^{+0.18}_{-4.85}$	-	<38.5
z6_23791	215.049250	52.997550	25.0	-21.5	$6.06^{+0.11}_{-0.10}$	-	<14.8
z6_30737	215.146750	53.050340	25.1	-21.6	$6.05^{+0.12}_{-0.12}$	-	<11.2
z6_37712	214.790480	52.781510	25.0	-21.6	$6.05^{+0.15}_{-0.16}$	-	<20.2
z6_5742	215.026260	52.881630	27.1	-	$5.95^{+0.69}_{-1.34}$	-	-
z6_48598	214.987770	52.896860	27.0	-	$5.84^{+0.37}_{-0.50}$	-	-
z6_66862	214.764580	52.810830	25.7	-	$5.79^{+0.25}_{-0.24}$	-	-

^a M_{UV} is estimated from the averaged flux over a 1450 – 1550Å bandpass from the best-fit galaxy SED model.

^b We present the 1σ range of z_{phot} .

^c Spectroscopic redshifts are estimated from the detected Ly α emission lines.

^d 3σ upper limits, measured from the median flux limits from individual spectra.

^e This object is not included in the analysis. We detected an emission line, but it is likely to be a low-redshift object from our SED fitting analysis.

References

- Bertin, E., & Arnouts, S. 1996, A&AS, 117, 393,
doi: [10.1051/aas:1996164](https://doi.org/10.1051/aas:1996164)
- Brammer, G. B., van Dokkum, P. G., & Coppi, P. 2008, ApJ, 686,
1503, doi: [10.1086/591786](https://doi.org/10.1086/591786)
- Brinchmann, J. 2022, arXiv e-prints, arXiv:2208.07467.
<https://arxiv.org/abs/2208.07467>
- Calzetti, D. 2001, New Astron., 45, 601,
doi: [10.1016/S1387-6473\(01\)00144-0](https://doi.org/10.1016/S1387-6473(01)00144-0)
- Castellano, M., Pentericci, L., Vanzella, E., et al. 2018, ApJL, 863,
L3, doi: [10.3847/2041-8213/aad59b](https://doi.org/10.3847/2041-8213/aad59b)
- Curtis-Lake, E., Carniani, S., Cameron, A., et al. 2022, arXiv
e-prints, arXiv:2212.04568. <https://arxiv.org/abs/2212.04568>
- Dayal, P., & Ferrara, A. 2018, PhR, 780, 1,
doi: [10.1016/j.physrep.2018.10.002](https://doi.org/10.1016/j.physrep.2018.10.002)
- Dayal, P., Volonteri, M., Choudhury, T. R., et al. 2020, MNRAS,
495, 3065, doi: [10.1093/mnras/staa1138](https://doi.org/10.1093/mnras/staa1138)
- Dijkstra, M. 2014, PASA, 31, e040, doi: [10.1017/pasa.2014.33](https://doi.org/10.1017/pasa.2014.33)
- Dijkstra, M., Wyithe, S., Haiman, Z., Mesinger, A., & Pentericci,
L. 2014, MNRAS, 440, 3309, doi: [10.1093/mnras/stu531](https://doi.org/10.1093/mnras/stu531)
- Endsley, R., & Stark, D. P. 2022, MNRAS, 511, 6042,
doi: [10.1093/mnras/stac524](https://doi.org/10.1093/mnras/stac524)

- Endsley, R., Stark, D. P., Charlot, S., et al. 2021a, *MNRAS*, 502, 6044, doi: [10.1093/mnras/stab432](https://doi.org/10.1093/mnras/stab432)
- Endsley, R., Stark, D. P., Chevillard, J., & Charlot, S. 2021b, *MNRAS*, 500, 5229, doi: [10.1093/mnras/staa3370](https://doi.org/10.1093/mnras/staa3370)
- Finkelstein, S., Bradac, M., Casey, C., et al. 2019, *BAAS*, 51, 221. <https://arxiv.org/abs/1903.04518>
- Finkelstein, S. L., Papovich, C., Salmon, B., et al. 2012, *ApJ*, 756, 164, doi: [10.1088/0004-637X/756/2/164](https://doi.org/10.1088/0004-637X/756/2/164)
- Finkelstein, S. L., Papovich, C., Dickinson, M., et al. 2013, *Nature*, 502, 524, doi: [10.1038/nature12657](https://doi.org/10.1038/nature12657)
- Finkelstein, S. L., Ryan, Jr., R. E., Papovich, C., et al. 2015, *ApJ*, 810, 71, doi: [10.1088/0004-637X/810/1/71](https://doi.org/10.1088/0004-637X/810/1/71)
- Finkelstein, S. L., Bagley, M., Song, M., et al. 2022, *ApJ*, 928, 52, doi: [10.3847/1538-4357/ac3aed](https://doi.org/10.3847/1538-4357/ac3aed)
- Finlator, K., Özel, F., Davé, R., & Oppenheimer, B. D. 2009, *MNRAS*, 400, 1049, doi: [10.1111/j.1365-2966.2009.15521.x](https://doi.org/10.1111/j.1365-2966.2009.15521.x)
- Grogin, N. A., Kocevski, D. D., Faber, S. M., et al. 2011, *ApJS*, 197, 35, doi: [10.1088/0067-0049/197/2/35](https://doi.org/10.1088/0067-0049/197/2/35)
- Hassan, S., & Gronke, M. 2021, *ApJ*, 908, 219, doi: [10.3847/1538-4357/abd554](https://doi.org/10.3847/1538-4357/abd554)
- Hoag, A., Bradač, M., Huang, K., et al. 2019, *ApJ*, 878, 12, doi: [10.3847/1538-4357/ab1de7](https://doi.org/10.3847/1538-4357/ab1de7)
- Horne, K. 1986, *PASP*, 98, 609, doi: [10.1086/131801](https://doi.org/10.1086/131801)
- Hu, W., Wang, J., Infante, L., et al. 2021, *Nature Astronomy*, doi: [10.1038/s41550-021-01322-2](https://doi.org/10.1038/s41550-021-01322-2)
- Hutchison, T. A., Walawender, J., & Kwok, S. H. 2020, in *Society of Photo-Optical Instrumentation Engineers (SPIE) Conference Series*, Vol. 11447, Society of Photo-Optical Instrumentation Engineers (SPIE) Conference Series, 114476A, doi: [10.1117/12.2562864](https://doi.org/10.1117/12.2562864)
- Inoue, A. K. 2011, *MNRAS*, 415, 2920, doi: [10.1111/j.1365-2966.2011.18906.x](https://doi.org/10.1111/j.1365-2966.2011.18906.x)
- Jung, I., Finkelstein, S. L., Dickinson, M., et al. 2019, *ApJ*, 877, 146, doi: [10.3847/1538-4357/ab1bde](https://doi.org/10.3847/1538-4357/ab1bde)
- . 2020, *ApJ*, 904, 144, doi: [10.3847/1538-4357/abbd44](https://doi.org/10.3847/1538-4357/abbd44)
- Jung, I., Papovich, C., Finkelstein, S. L., et al. 2022, *ApJ*, 933, 87, doi: [10.3847/1538-4357/ac6fe7](https://doi.org/10.3847/1538-4357/ac6fe7)
- Kannan, R., Garaldi, E., Smith, A., et al. 2022, *MNRAS*, 511, 4005, doi: [10.1093/mnras/stab3710](https://doi.org/10.1093/mnras/stab3710)
- Katz, H., Kimm, T., Haehnelt, M. G., et al. 2019, *MNRAS*, 483, 1029, doi: [10.1093/mnras/sty3154](https://doi.org/10.1093/mnras/sty3154)
- Koekemoer, A. M., Faber, S. M., Ferguson, H. C., et al. 2011, *ApJS*, 197, 36, doi: [10.1088/0067-0049/197/2/36](https://doi.org/10.1088/0067-0049/197/2/36)
- Kriek, M., Shapley, A. E., Reddy, N. A., et al. 2015, *ApJS*, 218, 15, doi: [10.1088/0067-0049/218/2/15](https://doi.org/10.1088/0067-0049/218/2/15)
- Kulkarni, G., Keating, L. C., Haehnelt, M. G., et al. 2019, *MNRAS*, 485, L24, doi: [10.1093/mnras/511/2/2025](https://doi.org/10.1093/mnras/511/2/2025)
- Kurucz, R. L. 1993, *SYNTHES* spectrum synthesis programs and line data
- Laporte, N., Meyer, R. A., Ellis, R. S., et al. 2021, *MNRAS*, 505, 3336, doi: [10.1093/mnras/stab1239](https://doi.org/10.1093/mnras/stab1239)
- Laporte, N., Ellis, R. S., Boone, F., et al. 2017, *ApJL*, 837, L21, doi: [10.3847/2041-8213/aa62aa](https://doi.org/10.3847/2041-8213/aa62aa)
- Larson, R. L., Finkelstein, S. L., Hutchison, T. A., et al. 2022, arXiv e-prints, arXiv:2203.08461. <https://arxiv.org/abs/2203.08461>
- Leonova, E., Oesch, P. A., Qin, Y., et al. 2022, *MNRAS*, 515, 5790, doi: [10.1093/mnras/stac1908](https://doi.org/10.1093/mnras/stac1908)
- Madau, P. 1995, *ApJ*, 441, 18, doi: [10.1086/175332](https://doi.org/10.1086/175332)
- Mason, C. A., & Gronke, M. 2020, *MNRAS*, 499, 1395, doi: [10.1093/mnras/staa2910](https://doi.org/10.1093/mnras/staa2910)
- Mason, C. A., Treu, T., Dijkstra, M., et al. 2018, *ApJ*, 856, 2, doi: [10.3847/1538-4357/aab0a7](https://doi.org/10.3847/1538-4357/aab0a7)
- Mason, C. A., Fontana, A., Treu, T., et al. 2019, *MNRAS*, 485, 3947, doi: [10.1093/mnras/stz632](https://doi.org/10.1093/mnras/stz632)
- Matsuoka, Y., Strauss, M. A., Kashikawa, N., et al. 2018, *ApJ*, 869, 150, doi: [10.3847/1538-4357/aace7a](https://doi.org/10.3847/1538-4357/aace7a)
- Matthee, J., Sobral, D., Gronke, M., et al. 2018, *A&A*, 619, A136, doi: [10.1051/0004-6361/201833528](https://doi.org/10.1051/0004-6361/201833528)
- McLean, I. S., Steidel, C. C., Epps, H. W., et al. 2012, in *Society of Photo-Optical Instrumentation Engineers (SPIE) Conference Series*, Vol. 8446, Ground-based and Airborne Instrumentation for Astronomy IV, ed. I. S. McLean, S. K. Ramsay, & H. Takami, 84460J, doi: [10.1117/12.924794](https://doi.org/10.1117/12.924794)
- McQuinn, M. 2016, *ARA&A*, 54, 313, doi: [10.1146/annurev-astro-082214-122355](https://doi.org/10.1146/annurev-astro-082214-122355)
- Mesinger, A., Aykutaalp, A., Vanzella, E., et al. 2015, *MNRAS*, 446, 566, doi: [10.1093/mnras/stu2089](https://doi.org/10.1093/mnras/stu2089)
- Mesinger, A., Furlanetto, S., & Cen, R. 2011, *MNRAS*, 411, 955, doi: [10.1111/j.1365-2966.2010.17731.x](https://doi.org/10.1111/j.1365-2966.2010.17731.x)
- Miralda-Escudé, J., & Rees, M. J. 1998, *ApJ*, 497, 21, doi: [10.1086/305458](https://doi.org/10.1086/305458)
- Morishita, T., Roberts-Borsani, G., Treu, T., et al. 2022, arXiv e-prints, arXiv:2211.09097. <https://arxiv.org/abs/2211.09097>
- Ocvirk, P., Lewis, J. S. W., Gillet, N., et al. 2021, arXiv e-prints, arXiv:2105.01663. <https://arxiv.org/abs/2105.01663>
- Ocvirk, P., Aubert, D., Sorce, J. G., et al. 2020, *MNRAS*, 496, 4087, doi: [10.1093/mnras/staa1266](https://doi.org/10.1093/mnras/staa1266)
- Oesch, P. A., van Dokkum, P. G., Illingworth, G. D., et al. 2015, *ApJL*, 804, L30, doi: [10.1088/2041-8205/804/2/L30](https://doi.org/10.1088/2041-8205/804/2/L30)
- Oke, J. B., & Gunn, J. E. 1983, *ApJ*, 266, 713, doi: [10.1086/160817](https://doi.org/10.1086/160817)
- Ouchi, M., Ono, Y., & Shibuya, T. 2020, *Annual Review of Astronomy and Astrophysics*, 58, 617, doi: [10.1146/annurev-astro-032620-021859](https://doi.org/10.1146/annurev-astro-032620-021859)
- Park, H., Jung, I., Song, H., et al. 2021, arXiv e-prints, arXiv:2105.10770. <https://arxiv.org/abs/2105.10770>
- Pentericci, L., Fontana, A., Vanzella, E., et al. 2011, *ApJ*, 743, 132, doi: [10.1088/0004-637X/743/2/132](https://doi.org/10.1088/0004-637X/743/2/132)

- Planck Collaboration, Ade, P. A. R., Aghanim, N., et al. 2016, *A&A*, 594, A13, doi: [10.1051/0004-6361/201525830](https://doi.org/10.1051/0004-6361/201525830)
- Qin, Y., Wyithe, J. S. B., Oesch, P. A., et al. 2021, arXiv e-prints, arXiv:2108.03675. <https://arxiv.org/abs/2108.03675>
- Rhoads, J. E., & Malhotra, S. 2001, *ApJL*, 563, L5, doi: [10.1086/338477](https://doi.org/10.1086/338477)
- Roberts-Borsani, G., Morishita, T., Treu, T., et al. 2022a, *ApJL*, 938, L13, doi: [10.3847/2041-8213/ac8e6e](https://doi.org/10.3847/2041-8213/ac8e6e)
- Roberts-Borsani, G., Treu, T., Mason, C., et al. 2022b, arXiv e-prints, arXiv:2207.01629. <https://arxiv.org/abs/2207.01629>
- Roberts-Borsani, G. W., Bouwens, R. J., Oesch, P. A., et al. 2016, *ApJ*, 823, 143, doi: [10.3847/0004-637X/823/2/143](https://doi.org/10.3847/0004-637X/823/2/143)
- Robertson, B. E. 2021, arXiv e-prints, arXiv:2110.13160. <https://arxiv.org/abs/2110.13160>
- Robertson, B. E., Ellis, R. S., Furlanetto, S. R., & Dunlop, J. S. 2015, *ApJL*, 802, L19, doi: [10.1088/2041-8205/802/2/L19](https://doi.org/10.1088/2041-8205/802/2/L19)
- Robertson, B. E., Tacchella, S., Johnson, B. D., et al. 2022, arXiv e-prints, arXiv:2212.04480. <https://arxiv.org/abs/2212.04480>
- Salmon, B., Papovich, C., Finkelstein, S. L., et al. 2015, *ApJ*, 799, 183, doi: [10.1088/0004-637X/799/2/183](https://doi.org/10.1088/0004-637X/799/2/183)
- Salpeter, E. E. 1955, *ApJ*, 121, 161, doi: [10.1086/145971](https://doi.org/10.1086/145971)
- Schaerer, D., Marques-Chaves, R., Barrufet, L., et al. 2022, arXiv e-prints, arXiv:2207.10034. <https://arxiv.org/abs/2207.10034>
- Smith, A., Kannan, R., Garaldi, E., et al. 2021, arXiv e-prints, arXiv:2110.02966. <https://arxiv.org/abs/2110.02966>
- Song, M., Finkelstein, S. L., Livermore, R. C., et al. 2016a, *ApJ*, 826, 113, doi: [10.3847/0004-637X/826/2/113](https://doi.org/10.3847/0004-637X/826/2/113)
- Song, M., Finkelstein, S. L., Ashby, M. L. N., et al. 2016b, *ApJ*, 825, 5, doi: [10.3847/0004-637X/825/1/5](https://doi.org/10.3847/0004-637X/825/1/5)
- Stark, D. P., Ellis, R. S., & Ouchi, M. 2011, *ApJL*, 728, L2, doi: [10.1088/2041-8205/728/1/L2](https://doi.org/10.1088/2041-8205/728/1/L2)
- Stark, D. P., Ellis, R. S., Charlot, S., et al. 2017, *MNRAS*, 464, 469, doi: [10.1093/mnras/stw2233](https://doi.org/10.1093/mnras/stw2233)
- Tilvi, V., Malhotra, S., Rhoads, J. E., et al. 2020, *ApJL*, 891, L10, doi: [10.3847/2041-8213/ab75ec](https://doi.org/10.3847/2041-8213/ab75ec)
- Trump, J. R., Arrabal Haro, P., Simons, R. C., et al. 2022, arXiv e-prints, arXiv:2207.12388. <https://arxiv.org/abs/2207.12388>
- Trussler, J. A. A., Adams, N. J., Conselice, C. J., et al. 2022, arXiv e-prints, arXiv:2207.14265. <https://arxiv.org/abs/2207.14265>
- van Leeuwen, F. 2007, *A&A*, 474, 653, doi: [10.1051/0004-6361:20078357](https://doi.org/10.1051/0004-6361:20078357)
- Wang, X., Cheng, C., Ge, J., et al. 2022, arXiv e-prints, arXiv:2212.04476. <https://arxiv.org/abs/2212.04476>
- Williams, H., Kelly, P. L., Chen, W., et al. 2022, arXiv e-prints, arXiv:2210.15699. <https://arxiv.org/abs/2210.15699>
- Yajima, H., Sugimura, K., & Hasegawa, K. 2018, *MNRAS*, 477, 5406, doi: [10.1093/mnras/sty997](https://doi.org/10.1093/mnras/sty997)
- Zheng, Z.-Y., Wang, J., Rhoads, J., et al. 2017, *ApJL*, 842, L22, doi: [10.3847/2041-8213/aa794f](https://doi.org/10.3847/2041-8213/aa794f)
- Zitrin, A., Labbé, I., Belli, S., et al. 2015, *ApJL*, 810, L12, doi: [10.1088/2041-8205/810/1/L12](https://doi.org/10.1088/2041-8205/810/1/L12)